On the Blending of the Landsat and MODIS Surface Reflectance: Predicting Daily Landsat Surface Reflectance

Feng Gao, *Member, IEEE*, Jeff Masek, Matt Schwaller, and Forrest Hall

Abstract—The 16-day revisit cycle of Landsat has long limited its use for studying global biophysical processes, which evolve rapidly during the growing season. In cloudy areas of the Earth, the problem is compounded, and researchers are fortunate to get two to three clear images per year. At the same time, the coarse resolution of sensors such as the Advanced Very High Resolution Radiometer and Moderate Resolution Imaging Spectroradiometer (MODIS) limits the sensors' ability to quantify biophysical processes in heterogeneous landscapes. In this paper, the authors present a new spatial and temporal adaptive reflectance fusion model (STARFM) algorithm to blend Landsat and MODIS surface reflectance. Using this approach, high-frequency temporal information from MODIS and high-resolution spatial information from Landsat can be blended for applications that require high resolution in both time and space. The MODIS daily 500-m surface reflectance and the 16-day repeat cycle Landsat Enhanced Thematic Mapper Plus (ETM+) 30-m surface reflectance are used to produce a synthetic "daily" surface reflectance product at ETM+ spatial resolution. The authors present results both with simulated (model) data and actual Landsat/MODIS acquisitions. In general, the STARFM accurately predicts surface reflectance at an effective resolution close to that of the ETM+. However, the performance depends on the characteristic patch size of the landscape and degrades somewhat when used on extremely heterogeneous fine-grained landscapes.

Index Terms—Data fusion, image enhancement, image processing, Landsat, Moderate Resolution Imaging Spectroradiometer (MODIS), remote sensing, surface reflectance.

I. INTRODUCTION

LANDSAT data have proven extremely useful in monitoring land cover and land-cover changes [1]–[3]. Recently, the Landsat ecosystem disturbance adaptive processing system (LEDAPS) was developed to create a Landsat-based surface reflectance product for North America to support the North American Carbon Program (NACP) [4]. Calibrated and atmospherically corrected surface reflectance is critical for the consistent retrieval of biophysical parameters and for detecting land-cover changes. However, the 16-day Landsat revisit cycle and frequent cloud contamination have limited the application of Landsat in detecting rapid surface changes that are crucial to

TABLE I
LANDSAT ETM+ BANDWIDTH AND MODIS BANDWIDTH

Landsat ETM+ Band	ETM+ Bandwidth (nm)	MODIS Land Band	MODIS Bandwidth (nm)
1	450-520	3	459-479
2	530-610	4	545-565
3	630-690	1	620-670
4	780-900	2	841-876
5	1550-1750	6	1628-1652
7	2090-2350	7	2105-2155

some applications such as crop-growth monitoring and detecting intraseasonal ecosystem disturbance.

One solution is to combine the spatial resolution of Landsat with the temporal frequency of coarse-resolution sensors, such as Moderate Resolution Imaging Spectroradiometer (MODIS). The Terra platform crosses the equator at about 10:30 A.M. local solar time, roughly 30 min. later than Landsat-7. Their orbital parameters are equal, and as such the viewing (near-nadir) and solar geometries are close to those of the corresponding Landsat acquisition. The Terra/Aqua MODIS provides frequent coarse-resolution observations, revisiting the globe once to twice per day. The MODIS observations include 250-m spatial resolution for red (band 1) and near-infrared [(NIR) band 2] wavebands and 500-m spatial resolution for other five MODIS land bands (band 3–7). The MODIS land bands have corresponding bandwidths to the Landsat Enhanced Thematic Mapper Plus (ETM+) sensor except their bandwidths are narrower than ETM+ (see Table I). In this paper, we use the MODIS daily 500-m surface reflectance product (MOD09GHK) to blend Landsat and MODIS data in order to produce a synthetic "daily" Landsat image. Such a product could have considerable utility for applications that require both high spatial resolution and frequent coverage.

Many studies have focused on the fusing of a fine-resolution panchromatic band and coarse-resolution spectral bands from one or more instruments [5]–[7]. The major purpose of those studies has been to generate high-resolution multispectral imagery combining the spectral characteristics of low-resolution data with the high spatial resolution of the panchromatic imagery. However, the outputs from those techniques were not calibrated to spectral radiance or reflectance. The traditional data fusing approaches such as those using hue saturation value (HSV) transforms, principal component analysis [7], and wavelet transformation [5], [6] may not suitable for the problem considered here, since we wish to capture the quantitative changes in radiometry (surface reflectance) caused by phenology.

In this paper, a spatial and temporal adaptive reflectance fusion model (STARFM) is presented to predict daily surface reflectance at Landsat spatial resolution and MODIS temporal frequency. The daily surface reflectance at Landsat spatial resolution is predicted from one or several pairs of Landsat and MODIS images acquired on the same day and one or more MODIS observations from the prediction date. The Landsat images can be "sparse" in time, letting the MODIS data capture temporal changes. Since Landsat surface reflectance is totally unknown for the predicted date, this approach works in an unsupervised style. The STARFM has been tested over forested areas, cropland regions, and heterogeneous mixtures of crop and forest. Results show that the STARFM can capture phenology changes precisely, although the accuracy depends on the characteristic patch size of the landscape.

Although MODIS and Landsat surface reflectances are used to test the STARFM algorithm, this approach is also applicable to other similar instruments in fusing fine spatial resolution and high-frequency temporal information. In particular, the next Landsat-like sensor [Operational Land Imager (OLI)] is slated to fly concurrently with the National Polar-Orbiting Operational Environmental Satellite System (NPOESS) Visible Infrared Imager/Radiometer Suite (VIIRS) global imager during the next decade. Algorithmic approaches such as those presented here will be especially valuable for obtaining the maximum value from both data streams.

II. APPROACHES

A. STARFM Theoretical Basis

Observations from different platforms first need to be calibrated and atmospherically corrected to surface reflectance so that they are comparable spatially and temporally. The LEDAPS has used the MODIS 6S approach for atmospheric correction of Landsat Thematic Mapper (TM) and ETM+ data, with the aerosol thickness derived from the imagery itself [4], [8]. Comparisons between MODIS and Landsat surface reflectance data reveal that they are very consistent [4]. However, due to the differences in data processing, acquisition time, bandwidth, and geolocation errors, small biases are expected.

Neglecting geolocation errors and differences in atmospheric correction, a heterogeneous coarse-resolution pixel at date t and surface reflectance (C_t) can be aggregated from finer resolution homogeneous pixels of surface reflectance F_t^i and percentage coverage A_t^i according to

$$C_t = \sum \left(F_t^i * A_t^i \right) \qquad (1)$$

where i refers to the spatial index (location) of the fine-resolution pixel. Even under the situation that percentage area A_t^i does not change and can be retrieved from previous or next acquisitions, the problem is still ill posed mathematically, and a unique solution cannot be determined without additional information. If F_t^i can be obtained from neighboring homogeneous coarse-resolution pixels, results could be improved dramatically. Therefore, the key to finding an approximate solution is to find spectrally similar homogeneous neighboring pixels.

For a homogenous pixel at a coarser MODIS resolution, the surface reflectance measured by Landsat data can be expressed as

$$L(x_i, y_j, t_k) = M(x_i, y_j, t_k) + \varepsilon_k \qquad (2)$$

where (x_i, y_j) is a given pixel location for both Landsat and MODIS images, t_k is the acquisition date for both MODIS and Landsat data, and ε_k represents the difference between observed MODIS and Landsat surface reflectance (caused by differing bandwidth and solar geometry). Here, we assume that the MODIS surface reflectance $M(x_i, y_j, t_k)$ has been previously georeferenced and super sampled to the resolution and bounds of the Landsat surface reflectance image $L(x_i, y_j, t_k)$ and thus shares the same image size, pixel size, and coordinate system. For simplicity, this assumption applies to all equations in the following text. Suppose we have n pairs input of $L(x_i, y_j, t_k)$ and $M(x_i, y_j, t_k)$ and each pair is acquired on the same date, where $k \in [1, n]$. The daily MODIS surface reflectance $M(x_i, y_j, t_0)$ at date t_0 is also a known value among inputs, then the predicted Landsat surface reflectance at date t_0 is

$$L(x_i, y_j, t_0) = M(x_i, y_j, t_0) + \varepsilon_0. \qquad (3)$$

Suppose the ground coverage type and system errors at pixel (x_i, y_j) does not change over prediction date t_0 and the date t_k, we will have $\varepsilon_0 = \varepsilon_k$ and thus

$$L(x_i, y_j, t_0) = M(x_i, y_j, t_0) + L(x_i, y_j, t_k) - M(x_i, y_j, t_k). \qquad (4)$$

However, this ideal situation cannot often be satisfied from MODIS and Landsat observations. Their relationships are complicated by several factors: 1) MODIS observation is not a homogeneous pixel and may include mixed land-cover types when considered at Landsat spatial resolution; 2) land cover may change from one type to another type during the prediction period; and 3) land-cover status (phenology) and solar geometry bidirectional reflectance distribution function (BRDF) changes will alter the reflectance from prediction date t_0 to date t_k.

By introducing additional information from neighboring pixels, we compute the surface reflectance for the central pixel at date t_0 with a weighting function

$$L\left(x_{w/2}, y_{w/2}, t_0\right) = \sum_{i=1}^{w} \sum_{j=1}^{w} \sum_{k=1}^{n} W_{ijk}$$
$$\times \left(M(x_i, y_j, t_0) + L(x_i, y_j, t_k) - M(x_i, y_j, t_k) \right) \qquad (5)$$

where w is the searching window size and $(x_{w/2}, y_{w/2})$ is the central pixel of this moving window. To ensure that the right information from neighbor pixels is used, only spectrally similar (i.e., from the same spectral class) and cloud-free pixels from Landsat surface reflectance within the moving window are used to compute the reflectance.

The weight W_{ijk} determines how much each neighboring pixel contributes to the estimated reflectance of the central pixel. It is very important and is determined by three measures as follows.

1) Spectral difference between MODIS and ETM+ data at a given location is

$$S_{ijk} = |L(x_i, y_j, t_k) - M(x_i, y_j, t_k)|. \qquad (6)$$

This is an approximate measure to determine the homogeneity of an MODIS pixel. The direct measure of homogeneity is limited by differences in projection and geolocation errors, and the actual MODIS pixel footprint is difficult to calculate. This approximation measures the difference between the Landsat observation and averaged neighboring pixels at coarse resolution. A smaller value of S_{ijk} implies that the fine spatial resolution pixel has closer spectral features to the averaged surrounding pixels; thus, the change at fine resolution should be comparable to that of the averaged surrounding pixels. Therefore, the pixel's reflectance should be assigned a higher weight in (5).

An extended assumption is that if MODIS and Landsat surface reflectances are equal at a given time, then these values should be equal for the prediction date. A special case is that of a homogeneous object at MODIS coarse resolution. There may be some cases where the Landsat surface reflectance equals the averaged surrounding values (MODIS surface reflectance) of a heterogeneous area, but their changes through time diverge. In that case, we need separate measures to minimize the bias. One approach is to use differences of MODIS observations during that period. The small changes of MODIS observations will ensure a better prediction on heterogeneous areas.

2) Temporal difference between the input and the predicted MODIS data is

$$T_{ijk} = |M(x_i, y_j, t_k) - M(x_i, y_j, t_0)|. \qquad (7)$$

This metric measures changes occurring between the prediction and the acquisition dates. A smaller T_{ijk} means less vegetation change between time t_k and t_0; thus, the pixel should be assigned a higher weight.

An extended assumption is that if the MODIS surface reflectance is constant over time, then the Landsat surface reflectance should not change as well. This is a reasonable assumption when we predict Landsat surface reflectance on the date of a given input pair. Thus, we will see the exact Landsat surface reflectance from predicted and observed data over a cloud-free area when the prediction date and the acquisition date are the same. This could be used to replace clouds and gaps from Landsat images. It will keep all cloud-clear Landsat observations from the same day while only replacing bad observations with predicted values.

However, if changes are too subtle to be detected by the MODIS observation, this algorithm will not be able to predict any change when synthesizing the fine resolution imagery. Also, there may be situations where the STARFM algorithm cannot detect changes when two contradicting changes occur within a coarse-resolution pixel simultaneously and compensate for each other.

3) Location distance between central pixel $(x_{w/2}, y_{w/2})$ and candidate pixel (x_i, y_j) at date t_k is

$$d_{ijk} = \sqrt{(x_{w/2} - x_i)^2 + (y_{w/2} - y_j)^2}. \qquad (8)$$

This measures the spatial distance between the central predicted pixel and the surrounding spectral similar candidate pixel. The spatial similarity is normally better for a closer pixel; thus, the closer candidate should be assigned a higher weight.

B. Implementation Considerations

The actual implementation of STARFM involves more detailed considerations on how to weigh spatial information. The weighting function needs to be adjusted depending on the complexity and heterogeneity of the study area.

1) Spectrally Similar Neighbor Pixels: As noted above (in Section II-A), the spectral similarity ensures that the correct spectral information is used from fine-resolution neighboring pixels. There are two ways to obtain spectrally similar pixels. An unsupervised classification can be performed before data blending, and pixels of same class are considered spectrally similar. The unsupervised classification should be applied to all fine-resolution (Landsat) images. These spectrally similar neighbor pixels could be different from date to date, which is useful in terms of capturing surface changes at fine resolution and thus allowing us to predict changes between dates. Another approach is to find spectrally similar pixels using thresholds in surface reflectance directly. The search process can be incorporated within the STARFM algorithm. In this paper, we used surface reflectance of red and NIR to determine the spectrally similar pixels. Differences of spectrally similar pixels are defined based on the standard deviation of fine-resolution images and the number of classes used. Using a large number of classes represents a stricter condition for selecting candidate neighbor pixels from fine-resolution images. Although our search process is similar to unsupervised classification, note that the purpose of the search process is to find pixels within the local moving window that are spectrally similar to the central pixel. Each central pixel becomes the center of the class, and the rules used to determine spectral similarity become local rules and thus vary from pixel to pixel. In contrast to the traditional classification, which applies the same classification rules over the whole region, our search process (second approach) will not be able to produce a unique classification map over the study area.

2) Combined Weighting Function: We use three factors in determining final weights for each spectrally similar pixel. They are based on the assumptions that: 1) coarse-resolution homogeneous pixels provide identical temporal changes as

fine-resolution observations from the same spectral class; 2) observations with less change from the prediction date provide better information for the prediction date; and 3) more proximal neighboring pixels normally provide better information for prediction. The final step is to combine these independent factors to create an ideal weight function that blends both temporal and spatial information.

First, we convert the actual distance to a relative distance through the function

$$D_{ijk} = 1.0 + d_{ijk}/A \qquad (9)$$

where A is a constant that defines the relative importance of the spatial distance to the spectral and temporal distance. The relative distance D_{ijk} within searching area "w" changes from 1 to $[1 + (1/\sqrt{2}) * (w/A)]$. A smaller value of A gives a larger dynamic range of D_{ijk}.

The combined spectral, temporal, and spatial distance can be computed with

$$C_{ijk} = S_{ijk} * T_{ijk} * D_{ijk} \qquad (10)$$

or in a logistic formula to make it less sensitive to the spectral differences

$$C_{ijk} = \ln(S_{ijk} * B + 1) * \ln(T_{ijk} * B + 1) * D_{ijk} \qquad (11)$$

where B is a scale factor (equal to $10\,000$ when using MODIS or LEDAPS reflectance products, which linearly scale reflectance from 0 to $10\,000$).

We use a normalized reverse distance as the weight function

$$W_{ijk} = (1/C_{ijk}) / \sum_{i=1}^{w} \sum_{j=1}^{w} \sum_{k=1}^{n} (1/C_{ijk}). \qquad (12)$$

If the MODIS surface reflectance does not change, we have $M(x_i, y_j, t_k) = M(x_i, y_j, t_0)$, then $T_{ijk} = 0$ and $C_{ijk} = 0$, and weight W_{ijk} is set to the maximum value. The predicted surface reflectance for central pixel of the moving window is then

$$L\left(x_{w/2}, y_{w/2}, t_0\right) = L(x_i, y_j, t_k).$$

This satisfies our basic assumption: if no change happens in the MODIS surface reflectance, then no change should be predicted at the Landsat spatial resolution. On the other hand, if the Landsat surface reflectance equals to the MODIS surface reflectance, we have $L(x_i, y_j, t_k) = M(x_i, y_j, t_k)$, then $S_{ijk} = 0$ and $C_{ijk} = 0$, and weight W_{ijk} is set to the maximum value. The predicted surface reflectance is

$$L\left(x_{w/2}, y_{w/2}, t_0\right) = M(x_i, y_j, t_0).$$

This satisfies our other basic assumption: if MODIS and Landsat surface reflectances are equal at date t_k, then they should be equal at date t_0.

3) Sample Filtering: After spectrally similar pixels from fine-resolution imageries are selected, additional filtering processes will then be applied to the candidates to remove poor-quality observations. First, all poor-quality data are excluded from candidates according to the QA layer in the Landsat and MODIS surface reflectance products. Second, neighbor pixels are filtered out if they cannot provide better spectral and spatial information than the central pixel of the moving window. A worse neighbor pixel normally cannot provide additional information on the prediction. A good candidate should satisfy the following condition:

$$S_{ijk} < \max\left(\left|L\left(x_{w/2}, y_{w/2}, t_k\right) - M\left(x_{w/2}, y_{w/2}, t_k\right)\right|\right) \qquad (13)$$

and

$$T_{ijk} < \max\left(\left|M\left(x_{w/2}, y_{w/2}, t_k\right) - M\left(x_{w/2}, y_{w/2}, t_0\right)\right|\right). \qquad (14)$$

However, since MODIS and Landsat surface reflectance values are derived from different processing chains, biases in geolocation and atmospheric correction are inevitable. Suppose we know that the uncertainties from Landsat and MODIS surface reflectance are σ_l and σ_m, respectively. All surface reflectance measurements are independent. The uncertainty for the spectral difference (6) between MODIS and ETM+ is

$$\sigma_{lm} = \sqrt{\sigma_l^2 + \sigma_m^2}.$$

The uncertainty for temporal difference (7) between two MODIS inputs is

$$\sigma_{mm} = \sqrt{\sigma_m^2 + \sigma_m^2} = \sqrt{2} * \sigma_m.$$

Considering the uncertainties in the candidate selection, (12) can be revised as

$$S_{ijk} < \max\left(\left|L\left(x_{w/2}, y_{w/2}, t_k\right) - M\left(x_{w/2}, y_{w/2}, t_k\right)\right|\right) + \sigma_{lm} \qquad (15)$$

and (13) can be revised as

$$T_{ijk} < \max\left(\left|M\left(x_{w/2}, y_{w/2}, t_k\right) - M\left(x_{w/2}, y_{w/2}, t_0\right)\right|\right) + \sigma_{mm}. \qquad (16)$$

Fig. 1 illustrates the overall flow of the STARFM algorithm. In the figure, only one input image pair (we normally use two in practice) is used as an example. Coarse-resolution data are first reprojected and resampled to the fine-resolution imagery. The three processes discussed above are applied to the fine resolution imagery to extract appropriate candidate pixels. Both coarse-resolution and fine-resolution data are then used in determining weights of candidates and finally to compute the predicted value. The predicted value in this diagram is closer to that of the upper-left pixel in the coarse-resolution matrix rather than the central pixel due to the contribution from spectrally similar neighbor pixels. If the central pixel of fine resolution is only used in prediction, we will likely obtain a predicted value
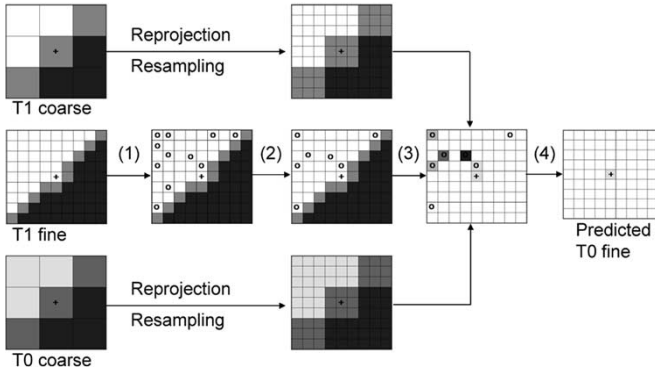
Fig. 1. Schematic diagram of STARFM approach. (Step 1) Fine-resolution data are first used to search for pixels (circles) that are spectrally similar to the central pixel (cross) within a moving window. These samples need to be filtered to ensure good selections (step 2). Both fine- and coarse-resolution data are then used in determining sample weights (step 3) according to the weighting function described in the text (dark color approximates heavier weight). Finally, the prediction value is computed from these weighted values with (5), step 4.

similar to the central pixel of the coarse-resolution matrix and thus lose the fine spatial resolution information.

III. ALGORITHM TESTS WITH SIMULATED DATA

A. Retrieving Changing Reflectance

Simulated reflectance data allow us to explore the behavior of the STARFM algorithm and assess its strengths and limitations. In this simple case, there are only two objects (water and vegetation, for example) included in Fig. 2. The shapes of water and vegetation are fixed, and we assume that the water body (circle) has a constant surface reflectance of 0.05 over the observing period, while the vegetation reflectance changed from 0.1 [Fig. 2(a)] to 0.2 [Fig. 2(b)] and then to 0.4 [Fig. 2(c)]. The MODIS-like 500-m spatial resolution images [Fig. 2(d)–(f)] were aggregated from the Landsat-like 30-m spatial resolution images [Fig. 2(a)–(c)], respectively. Using the STARFM algorithm and data from Fig. 2(a) and (c)–(f), we predicted finer resolution data for [Fig. 2(b)]. When the surrounding spatial information at finer resolution data is used, a nearly exact view [Fig. 2(g)] can be retrieved at finer resolution for this simple case. However, if we neglect additional spatial information from Fig. 2(a) and (c) and only use information from the central pixel, the MODIS cell boundaries from coarse resolution data will appear in the prediction [Fig. 2(h)]. This example reveals the importance of additional fine-resolution spatial information from surrounding spectrally similar pixels.

B. Retrieving Changing Shapes

Land cover may change over a growing season, not just in terms of overall spectral reflectance but also in terms of shape and size. Particular land-cover types may expand (e.g., ephemeral lakes) or disturbance events (e.g., burns) may alter the landscape composition. To better understand the STARFM algorithm's performance, we assume that the surface reflectance is constant with time for two land-cover types, a background at $r = 0.4$ and a circular object at $r = 0.1$. The
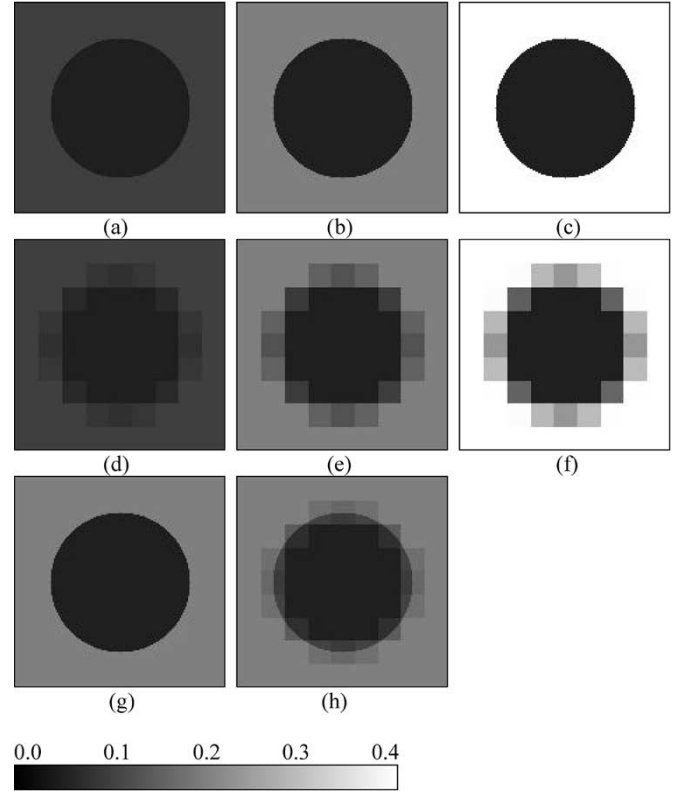

Fig. 2. Test of the STARFM algorithm using a simulation of temporal changes for water (inside circle) and vegetation (outside the circle), assuming that the water has a constant reflectance of 0.05 over the period, while the vegetation part changes reflectance from 0.1 (a) to 0.2 (b) and then to 0.4 (c). The coarse-resolution MODIS-like images (d), (e), and (f) are aggregated from the Landsat-like fine spatial resolution images (a), (b), and (c), respectively. The object is to use the MODIS time series and fine-resolution views (a) and (c) to retrieve view (b). A nearly exact match (g) can be retrieved at fine resolution with additional information from surrounding spectrally similar pixels. However, if no additional spatial information is used, the MODIS cell boundaries from coarse-resolution data will appear in the prediction (h).

circular object changes radius from 500 m [Fig. 3(a) and (d)] to 1000 m [Fig. 3(b) and (e)] and then 2000 m [Fig. 3(c) and (f)]. Fig. 3(a)–(c) shows the simulated Landsat-like 30-m spatial resolution data. The MODIS-like 500-m-resolution data Fig. 3(d)–(f) are aggregated from the Landsat-resolution views. Fig. 3(g) is the predicted image from finer resolution data [Fig. 3(a) and (c)] and coarse-resolution data [Fig. 3(d)–(f)] with an additional neighbor pixel spatial-information option turned on. The predicted image captures the changed area from Fig. 3(a) and the unchanged area from Fig. 3(c). The area between is smoothed with a reasonable approximation to the shape of the circle. Fig. 3(h) is the absolute difference between true [Fig. 3(b)] and predicted data [Fig. 3(g)]. It shows that differences are greatest along the border of the circular region, where the spatial resolution of the STARFM prediction cannot exactly match that of the original high-resolution image.

C. Retrieving Small Objects

As shown in Fig. 2, STARFM can retrieve both shape and reflectance if there exist "pure" (homogeneous) coarse-resolution neighboring pixels. However, prediction errors could be large if no such pixel exists.

Fig. 4. Prediction errors change with the actual object size. Larger objects (radius > 330 m) can be predicted very accurately while using both spectrally similar surrounding spatial information and weighting function.
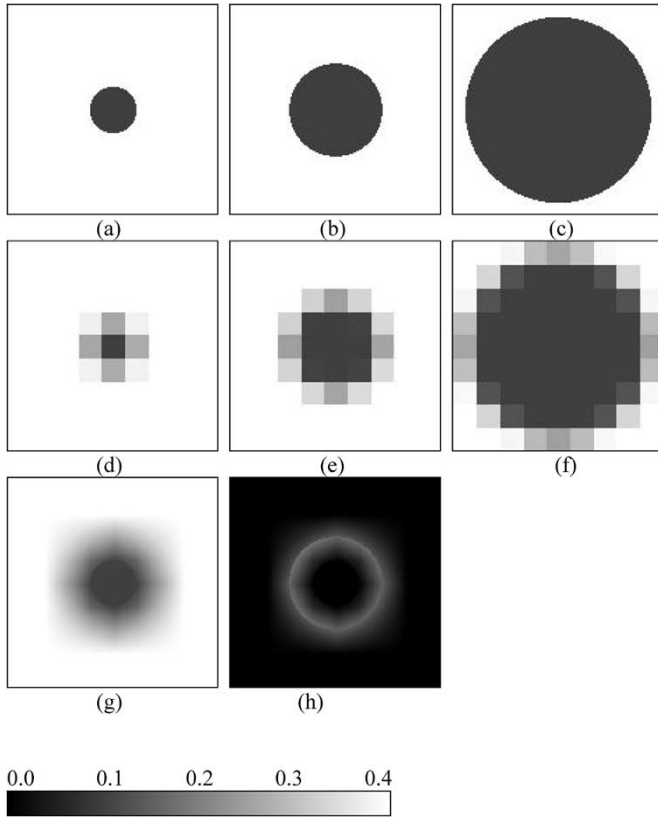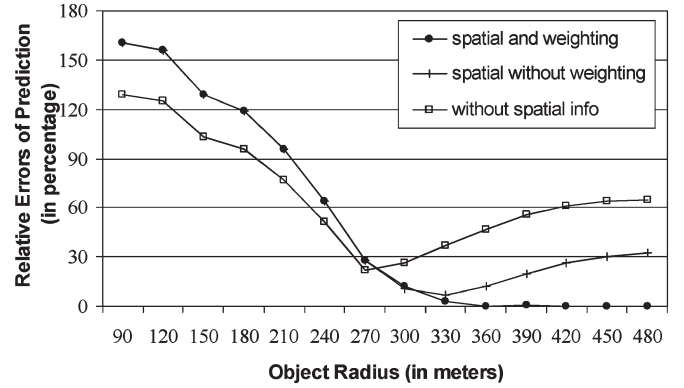
Fig. 3. Simulation test on a changing object. Suppose surface reflectance is 0.4 for the background and 0.1 for the changing object. Radii of the circles are 500, 1000, and 2000 m for (a), (b), and (c), respectively. The MODIS-like 500-m-resolution data (d), (e), and (f) are aggregated from the Landsat-like 30-m simulation data (a), (b), and (c), respectively. Figure (g) is the predicted image from finer resolution data (a) and (c) and coarse-resolution data (d), (e), and (f). Figure (h) is the difference between true (b) and predicted data (g).

Similar to the previous simulation in Fig. 2, we assume that a water body (circle) has a constant surface reflectance of 0.05. The background vegetation (outside the circle) changes reflectance from 0.1 ($t1$) to 0.2 ($t2$) and then 0.4 ($t3$) for three different periods. We use simulated fine-resolution images from $t1$ and $t3$ and coarse-resolution images from $t1$, $t2$, and $t3$ to compute fine-resolution reflectance at $t2$. The predicted pixels are then compared with the "actual" data on $t2$ (truth). The relative difference in percentage (overall error) is computed for each prediction for a changing radius from 90 to 480 m.

Fig. 4 shows that the prediction error decreases as the retrieved object becomes larger if both spectrally similar surrounding spatial information and the weighting function are used. Once the object size reaches the MODIS 500-m pixel size (object radius $= 500 * \sqrt{(2)}/2 = 353.3$ m), errors are reduced dramatically to less than 1% due to the contribution from "pure" neighboring MODIS pixels. However, if we use uniform weights for all spectrally similar neighbor pixels (no weighting function), results are similar for the smaller objects (radius < 330 m) but worse for larger objects (radius $\geq$ 330 m) compared to the approach using both surrounding spatial information and the weighting function. An interesting trend in Fig. 4 is that for smaller objects (radius < 300 m), the algorithm only using the central pixel (without using surrounding spatial information)

actually gets better results. This may due to the fact that neighboring pixels of a small object (radius < 300 m) cannot provide additional useful information for the prediction. Including such information in the prediction may make the prediction worse. This example also shows how important it is to choose good candidates for the computation as discussed above. It is better to exclude pixels in the computation if their inclusion cannot provide additional information. Another way to deal with small objects is to increase the size of the searching window size and look for "pure" coarse-resolution pixels over a larger area. Once such "pure" pixels are found, the prediction can be significantly more accurate.

D. Retrieving Linear Objects

Linear objects such as roads and small rivers are normally visible in fine-resolution Landsat imagery but are not obvious in coarse-resolution MODIS imagery. Fig. 5(a)–(c) represents simulated Landsat-like images with background changing from 0.1 [Fig. 5(a)] to 0.2 [Fig. 5(b)] and then 0.4 [Fig. 5(c)]. The simulated water body (circle) has a constant reflectance of 0.05. The simulated road (over background) and bridge (over water) have a constant reflectance of 0.5. The MODIS-like data in Fig. 5(d)–(f) are aggregated from the Landsat-like data. Roads (over background) are still visible in Fig. 5(d) and (e) but not in Fig. 5(f) due to the smaller contrast of roads and the background in Fig. 5(c). Fig. 5(g) is a predicted version of Fig. 5(b) using fine-resolution images [Fig. 5(a) and (c)] and coarse resolution imageries [Fig. 5(d)–(f)] with an additional neighbor pixel spatial-information option turned on. The bridge (segment within circle) in Fig. 5(g) is retrieved perfectly due to the stable water background. Roads (segments outside circle) in Fig. 5(g) are retrieved imperfectly (reflectances vary depending on the location and are less than 0.5), which is due to the changing reflectance surrounding line and smaller contrast between the road and the background.

IV. APPLICATIONS

In this section, we apply the STARFM algorithm to actual Landsat-7 and MODIS imagery. The standard MODIS daily
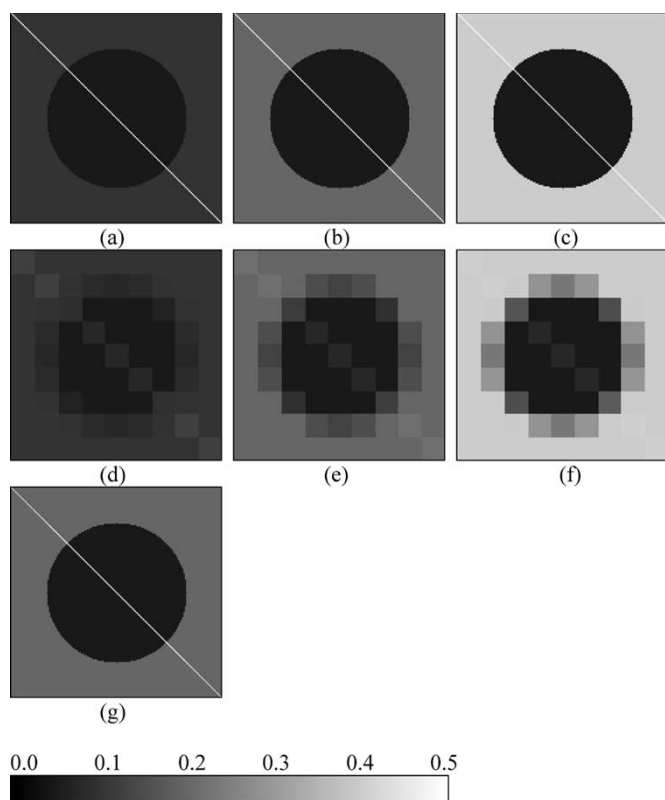
Fig. 5. Simulation test on a linear object. The MODIS-like resolution data (d), (e), and (f) are aggregated from the Landsat-like data (a), (b), and (c), respectively. Imagery (g) is predicted from fine-resolution imageries (a) and (c) and coarse-resolution imageries (d), (e), and (f). A bridge (segment within circle) in (g) is predicted perfectly. Roads (segments outside circle) in (g) are predicted but are not perfect values.

surface reflectance data include 250-m, 500-m, and 1-km-resolution products [8]. The 500-m-resolution product includes all seven MODIS land bands (red and NIR bands are aggregated from the 250-m resolution). The multiple-date composite surface reflectance is generated from daily surface reflectance products, with the eight-day composite surface reflectance product primarily including high-quality nadir view observations [8]. The nadir BRDF-adjusted reflectance (NBAR) is retrieved from cloud-clear observations during a 16-day period with a semiempirical BRDF [9]. In this study, we used daily a 500-m surface reflectance (MOD09GHK) as an example to demonstrate our approach to blend the fine spatial resolution data with temporal frequent coarse-resolution data.

A. Seasonal Changes Over Forested Region

A selection of MODIS and Landsat data was acquired for the Boreal Ecosystem–Atmosphere Study (BOREAS) southern study area (54° N, 104° W), where the growing season is short and phenology changes are extreme. MODIS daily surface reflectance images at a 500-m spatial resolution (MOD09GHK product) were acquired for late May through late September 2001. Landsat-7 ETM+ images were acquired for four dates during this period: May 24, 2001, July 11, 2001, August 12, 2001, and September 29, 2001. Scene subsets are shown in Fig. 6 using a NIR-red-green as red-green-blue composite and identical linear stretches. The upper row shows the MODIS

imagery, and the lower row shows the Landsat imagery. Note that the MODIS and Landsat surface reflectance images are very similar for same-day observations.

The major land-cover type in this region is forest (spruce, pine, aspen), with subsidiary fen and patches of sparse vegetation (soil, rock, burn scars). Land-cover patches are large; for most surface types, a homogeneous pixel at the MODIS resolution can be found. Land-cover changes are also small during this short observation period—most spectral changes are caused by phenology and changing solar zenith angle. Thus, the area is a relatively simple example for testing. We select 1500 m × 1500 m as the moving window size, which is 3 × 3 MODIS 500-m-resolution pixels or 50 × 50 Landsat 30-m-resolution pixels. The direct combination weighting function (10) is used in this example. The range of location relative distance are defined, varying from 1 to 2.4 ($A = 750$ m). The uncertainties of Landsat and MODIS surface reflectance are set as 0.002 and 0.005 for the visible band and the NIR band, respectively.

Fig. 7 shows the predicted surface reflectance (bottom) at Landsat spatial resolution from same-day MODIS images (upper row) and ETM+/MODIS image pairs in Fig. 6. For example, the June 4 data are computed with input image pairs from May 24 and July 11, as well as the MODIS image acquired on June 4. The rest are computed with input image pairs from August 12 and September 29. The predicted image captures rapid phenology changes from MODIS data while retaining the Landsat spatial details. Clear land and water boundaries can be predicted due to the additional spatial information from neighboring pixels. Linear objects such as roads are obvious in the predicted images as seen in the simulation tests.

We use the July 11 Landsat surface reflectance image as a validation source and use May 24 and August 12 to predict the July 11 image. Fig. 8(a) is the observed surface reflectance, and Fig. 8(b) is the predicted surface reflectance for the NIR band (Landsat band 4). The difference image [Fig. 8(c)] between prediction and observation shows that the differences between prediction and observation are very small. Note that, since the observations of July 11 and August 12 are both acquired during peak vegetation greenness, these are already very close in Fig. 6 (two central images). As such, this may not be the strictest test of the STARFM algorithm performance. Nevertheless, we still see some improvements from the scatter plots in Fig. 9. Fig. 9(a) and (c) shows the correlation between the actual July 11 and August 12 reflectance images, for the red and NIR bands, respectively. Both scatter plots deviate from the 1–1 line, although the two images look very close visually (Fig. 6), indicating some changes in phenology during this one-month interval. Fig. 9(b) and (d) shows the scatter plots of July 11 and the predicted surface reflectance for red and NIR, respectively. These data fall closer to the 1–1 line, indicating that the STARFM algorithm captures and adjusts for some of these phenology changes. The linear fitting gains are 0.830 and 0.955 for Fig. 9(a) and (b), respectively, and are 0.941 and 1.004 for Fig. 9(c) and (d), respectively. The R square between prediction and actual observations are slightly smaller than that from July 11 and August 12, which may be caused by some mixed pixels in the prediction.
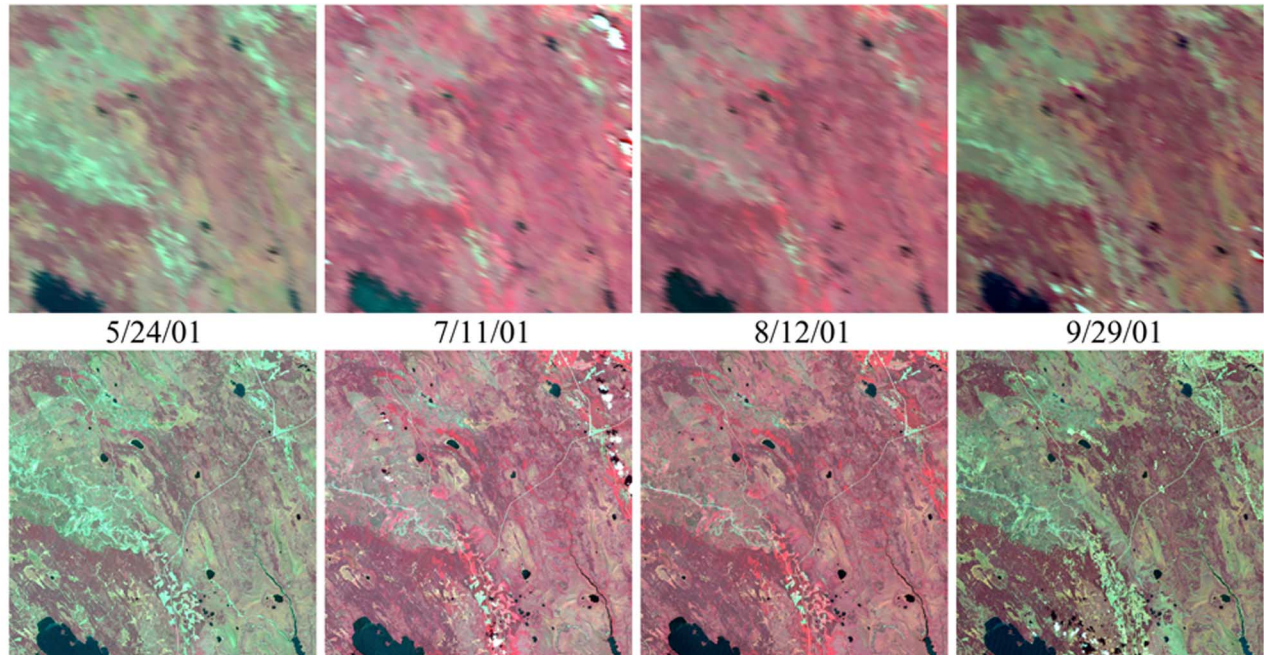
Fig. 6.   MODIS composited surface reflectance (upper row) and Landsat surface reflectance (lower row) images. From left to right, they were acquired from May 24, 2001 (day of year: 144), July 11, 2001 (192), August 12, 2001 (224), and September 29, 2001 (272), respectively. The images are 36 km × 36 km in size.
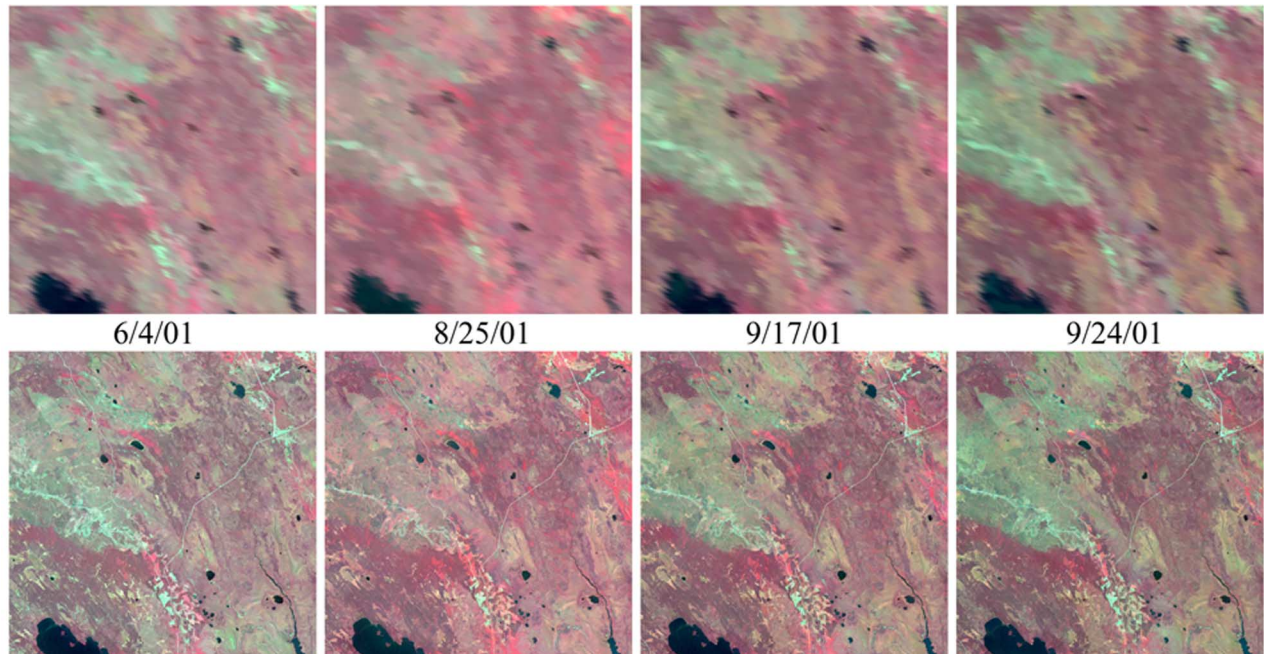

Fig. 7.   Predicted surface reflectance (bottom) from MODIS reflectance imagery (upper row) and Landsat/MODIS imagery pairs shown in Fig. 6. The predictions capture rapid phenology changes from MODIS data while retaining spatial detail derived from Landsat. Clear land and water boundary and roads are obvious in the predicted images.

Table II shows the average differences and absolute differences of surface reflectance between the actual (observed) Landsat surface reflectance on July 11, the observed surface reflectance from bracketing dates, and the results of the STARFM prediction for July 11. The predicted surface reflectance has the smallest difference for all bands, which implies that the STARFM algorithm gained information from MODIS obser-

vations and correctly adjusted for the phenology/BRDF differences between the July 11 and August 12 images.

B. Cropland Development

Cropland patches are small and normally show distinct temporal patterns based on planting/harvest schedules and local
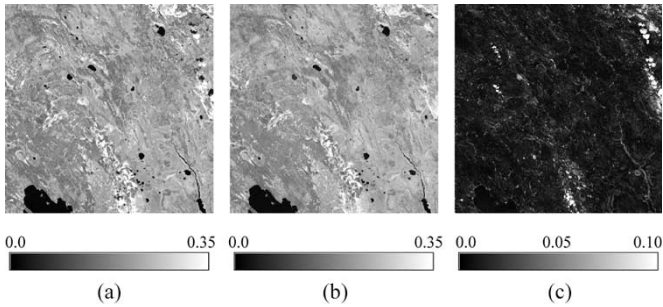
Fig. 8. Actual observation of (a) July 11 and prediction of (b) July 11 from May 24 and August 12 for NIR band (Landsat band 4), and the corresponding absolute difference image (c) shows a very good agreement. Note that the large differences (bright color) in (c) are caused by cloud contaminations.
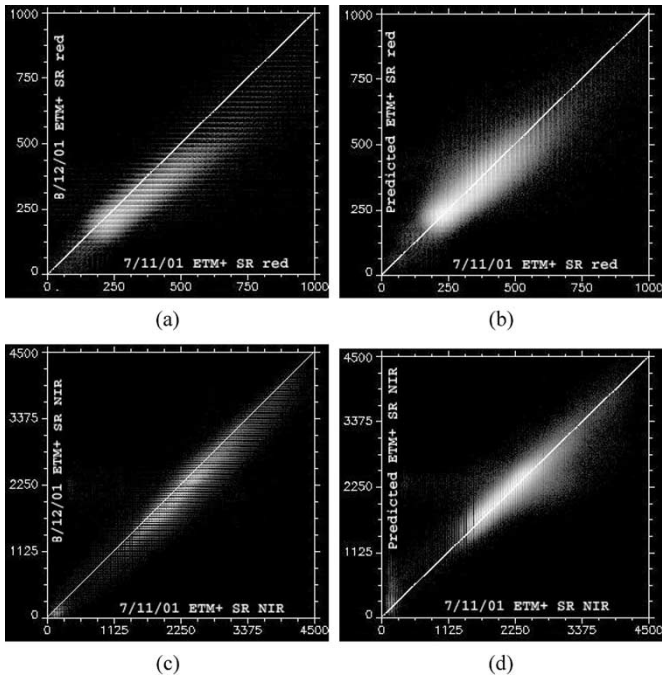

Fig. 9. Scatter plots of July 11 and predicted surface reflectance (scale factor = 10 000) for (b) red and (d) NIR shows a better fit to 1-to-1 line than scatter plots of July 11 and August 12 surface reflectance for (a) red and (c) NIR, which reveals that the STARFM algorithm captures some phenology changes from July 11 to August 12.

TABLE II
AVERAGE DIFFERENCES AND ABSOLUTE DIFFERENCES OF MAY 24, AUGUST 12, AND PREDICTED SURFACE REFLECTANCE COMPARED TO JULY 11 SURFACE REFLECTANCE

| ETM+ Band	Reflectance 7/11/01	Absolute Differences			Differences		
		5/24/01	8/12/01	Prediction	5/24/01	8/12/01	Prediction
1	0.0275	0.0055	0.0045	0.0033	-0.0055	0.0035	0.0019
2	0.0469	0.0043	0.0071	0.0035	-0.0014	0.0070	-0.0002
3	0.0339	0.0114	0.0058	0.0044	-0.0111	0.0053	0.0012
4	0.2207	0.0443	0.0155	0.0129	0.0441	0.0140	-0.0030
5	0.1355	0.0130	0.0164	0.0103	-0.0078	0.0158	-0.0031
7	0.0606	0.0165	0.0072	0.0078	-0.0157	0.0059	-0.0017
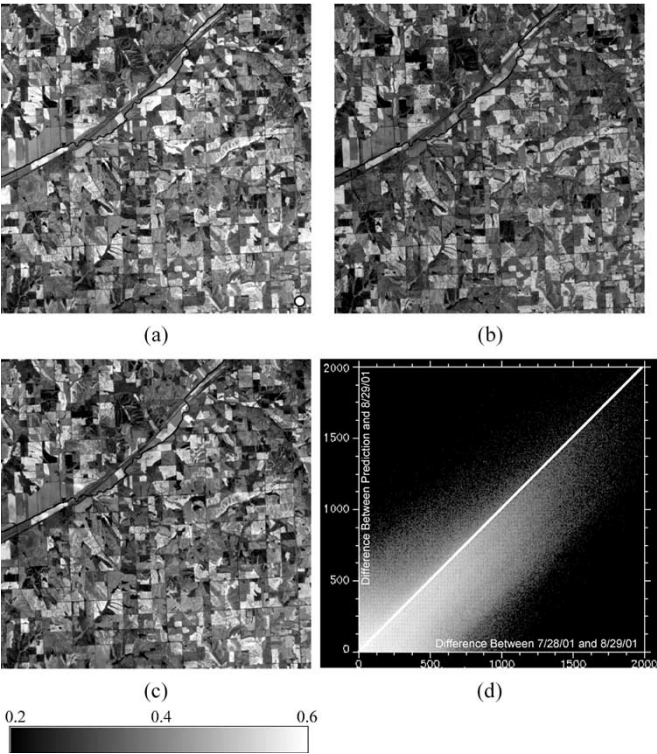
Fig. 10. Predicted surface reflectance of August 29, 2001 (c) from the July 28, 2001 image (a) for NIR band shows that it captures cropland temporal changes comparing to the actual observation on August 29, 2001 (b). Scatter plot (d) shows the absolute differences between the predicted surface reflectance, and actual observations are less than the absolute differences between July 28, 2001 and August 29, 2001 observations in the NIR band (scale factor = 10 000). Circle in (a) shows the coverage of a 500-m MODIS nadir observation. The displayed subset of image is about 17 km × 17 km.

environmental conditions such as soil water content, nutrition, and health. Monitoring crop growth requires both high spatial resolution imagery (to isolate particular fields) and high temporal resolution imagery (to track development). Thus, this application represents a good use of the STARFM algorithm.

Fig. 10 shows a selected agriculture test area from western Iowa (42.1° N, 95.7° W). Fig. 10(a) and (b) shows maps of the NIR band from July 28, 2001 and August 29, 2001, respectively. We used one input pair (Landsat and MODIS surface reflectance on July 28, 2001) and the MODIS 500-m-resolution surface reflectance of August 29 to predict Landsat spatial resolution surface reflectance from August 29. Fig. 10(c) is the predicted surface reflectance of July 18 for the NIR band. Most of temporal changes of the bright targets in Fig. 10(a) have been adjusted. The scatter plot [Fig. 10(d)] shows the absolute difference between the predicted surface reflectance and the actual observation (July 28, 2001) and the absolute difference

between the July 28, 2001 and August 29, 2001 observations in the NIR band. Since the difference between predicted and actual surface reflectance is less than the difference between the subsequent dates, additional temporal information from MODIS observations have been leveraged.

As shown in our previous simulation tests, prediction errors can be minimized dramatically if there exist "pure" coarse resolution pixels. Even though this test area is cropland, the temporal-spectral patterns differ from patch to patch. There are very few patches that can contain a "pure" MODIS sized pixel [shown as a circle in Fig. 10(a)]. The mixed coarse-resolution pixels decrease the dynamic range of surface reflectance due to the spatial aggregation; therefore, the predictions will have a smaller dynamic range as well. Small patches with very high or very low surface reflectance will most likely have larger prediction errors.

Fig. 12. Predicted surface reflectance from Virginia test area shown in Fig. 11 from simulated coarse-resolution data at (a) 500-m, (b) 750-m, and (c) 1-km spatial resolutions for the red band.
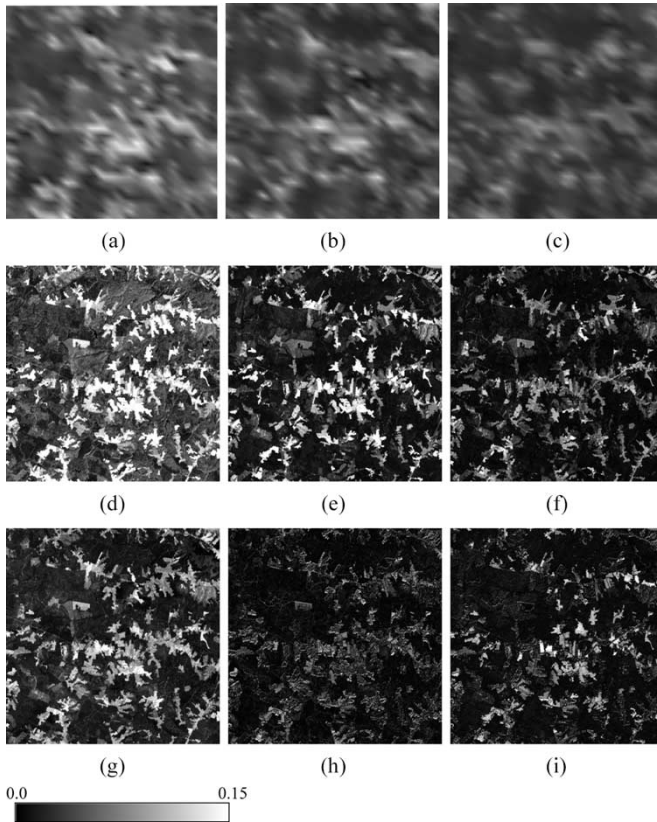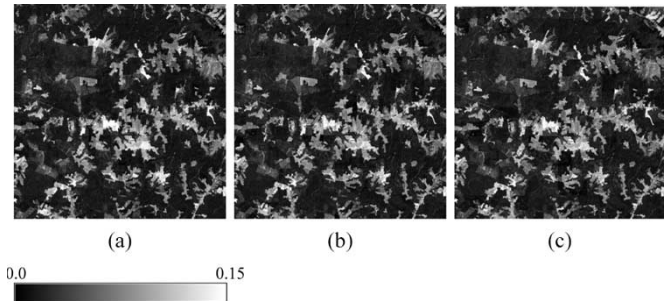

Fig. 11. Test on a mixture area in the central of Virginia (path 15 row 34) where evergreen forests, deciduous forests, and croplands show different growing patterns from (a), (d) February 7 to (b), (e) May 30 and to (c), (f) July 17 on both MODIS [(a), (b), and (c)] and Landsat [(d), (e), and (f)] maps (demonstrated with the red band). The predicted surface reflectance (g) from the MODIS surface reflectance [(a), (b), and (c)] and the Landsat surface reflectance [(d) and (f)] captures most features of the forest phenology from (f) and the cropland phenology from (d) comparing to the actual Landsat observation (e). The absolute difference (h) of the surface reflectance in the red band between prediction and observation of May 30 is mostly less than the absolute difference (i) between observations of May 30 and July 17, which implies that additional temporal information from MODIS observations have been gained in the prediction.

C. Complex Mixture Regions

Complex mixtures of land-cover type are a challenge for all methods of data fusion. Fig. 11 shows a small subset region (15 km × 15 km) from the eastern Virginia scene (38° N, 77° W). This region includes deciduous forest, evergreen forest, mixed forest, and some cropland. Three acquisition dates (February 7, 2001, May 30, 2001, and July 17, 2001) were used in this example. Corresponding 500-m-resolution daily MODIS surface reflectance images were reprojected and were subsets to the Landsat scene. Three temporal patterns are very clear in this region. The evergreen forest has the constant reflectance from early February [Fig. 11(d)] to late May [Fig. 11(e)] and middle July [Fig. 11(f)], while the deciduous forest shows green-up on late May [Fig. 11(e)] imagery, and the cropland shows green-up on middle July [Fig. 11(f)]. Therefore, the late May image [Fig. 11(e)] contains evergreen-forest reflectance information from both February [Fig. 11(d)] and July [Fig. 11(f)] imagery. It also contains cropland reflectance information mostly from the February image [Fig. 11(d)] and deciduous-forest informa-

tion mostly from the July image [Fig. 11(f)]. This test area demonstrates not only the complex phenology of different land-cover types but is also composed of very small patches of these differing types.

Considering the complexity of the test region and the fact that homogeneous MODIS pixels are not often found, we increased our search windows to 6000 m and used a stronger location distance function ($A = 250$ m) to give more proximal homogenous pixels a stronger weight in the algorithm. We used logistic weighting function (11) in this test to decrease contributions caused by spectral differences. The uncertainty of surface reflectance is also higher for a heterogeneous area due to the frequency of mixed pixels. We set reflectance uncertainty to 0.01 for visible bands and 0.015 for NIR bands.

Fig. 11(g) is the predicted surface reflectance in red band for May 30 from the MODIS surface reflectance [Fig. 11(a)–(c)] and Landsat surface reflectance [Fig. 11(d) and (f)]. Compared to the actual observations in Fig. 11(e), the predicted surface reflectance successfully captures most of phenology patterns of evergreen forests from early February [Fig. 11(d)] and July [Fig. 11(f)], most of the cropland pattern from the early February image [Fig. 11(d)], and most of the deciduous forest patters from the July image [Fig. 11(f)]. Fig. 11(h) shows the absolute differences in red band between prediction and observation of May 30. The difference in Fig. 11(h) is mostly less than the absolute difference of observations between May 30 and July 17 [Fig. 11(i)], since additional temporal information have been gained from MODIS observations.

In order to further investigate the uses of this algorithm in complex regions, we simulated coarse-resolution data sets from Landsat surface reflectance to make "perfectly" matching coarse-resolution data sets in 500-m, 750-m, and 1-km spatial resolutions. Fig. 12 shows the predicted surface reflectance in red band from the simulated coarse-resolution data. The three predictions from different coarse-resolution data are very close.

Table III shows the average prediction errors from 500-m MODIS data and four simulations (250 m, 500 m, 750 m, and 1 km) for red and NIR bands. The results show that differences among predictions with coarse resolution greater than 500 m are small, although some improvement occurs in terms of absolute differences and standard deviation by using 250-m resolution data. The prediction using 1-km simulation data is very close to the prediction from actual 500-m MODIS

Data Sources	Absolute Difference		Difference		Standard Deviation	
	red	NIR	red	NIR	red	NIR
500m MODIS	0.0166	0.0461	-0.0013	-0.0028	0.0263	0.0599
250m Sim	0.0128	0.0351	0.0021	-0.0054	0.0223	0.0475
500m Sim	0.0146	0.0410	0.0010	-0.0043	0.0242	0.0543
750m Sim	0.0155	0.0444	0.0011	-0.0041	0.0254	0.0584
1km Sim	0.0162	0.0462	0.0013	-0.0035	0.0263	0.0605

data. Part of reasons is that the geolocation precision is crucial for this complex area. A small shift of pixel location will confuse the temporal response and affect the prediction. The simulated 1-km coarse-resolution data have perfect geolocation compared to the Landsat imagery, while the MODIS 500-m data do not. The STARFM algorithm is not very sensitive to the coarse-resolution data for this complex area. As expected, the prediction accuracy for this complex area is not as good as in Table II for a large forest area. Finer coarse-resolution data are required to provide "pure" coarse-resolution pixels and thus provide "correct" temporal information for the fine resolution data.

V. CONCLUSION AND DISCUSSION

Landsat 30-m-resolution observations have been widely used in regional land-cover mapping and change detection. Applications of Landsat imageries are unfortunately limited by 16-day repeat cycling and cloud contaminations. On the other hand, the Terra/Aqua MODIS observations cover the globe one or two times each day but lack fine spatial resolution. The STARFM algorithm that we developed in this paper uses spatial information from fine-resolution imagery and temporal information from coarse-resolution imagery to produce estimates of surface reflectance that are high resolution in both space and time. In essence, the collection of daily MODIS imagery and seasonal Landsat imagery allow the generation of synthetic "daily" Landsat-like views. This algorithm can be expanded to other similar data fusion applications given observations that can be corrected to comparable surface reflectance values.

The STARFM can produce extremely accurate estimates of high-resolution reflectance that preserve the high spatial resolution of Landsat and high temporal resolution of MODIS if "pure" coarse-resolution neighbor pixels can be found within the moving window. For complex mixtures of different land-cover types, the adjustment of algorithm parameters such as the size of the searching window and the weighting function (direct or logistic) can improve prediction. However, the algorithm ultimately requires daily data at a finer resolution than 500 m for these heterogeneous "fine grained" regions.

Although STARFM works with one input Landsat and MODIS pair, the prediction can be improved if more than one pair is used. For estimating the annual growing cycle, results are improved if Landsat imagery is available at the beginning (greenup), middle (maturity), and end (senescence) of the growing season. Thus, the Landsat data act as phenology "transition points" that bracket the temporal interpolation. The algorithm has proven very robust in capturing phenology and BRDF changes across large areas.

The simulation tests show that the STARFM can capture the initial and final states of changing shapes and thus can capture disturbance and land-cover change processes. If changes are "permanent" during the growing season (such as burn scars and land-cover conversion), the algorithm should be able to record the transition from one state to another as demonstrated in the simulation tests. However, if changes are transient and not recorded in any of the bracketing Landsat images (e.g., clouds), then it may not be possible to capture them in fine resolution. In addition, any changes that are too subtle to be observed by the MODIS observations are not predictable with this algorithm.

Although the work in this paper is based on the MODIS and Landsat surface reflectance, the STARFM approach is also applicable to future instrument suites, such as the Landsat Data Continuity Mission OLI and the NPOESS VIIRS. The former is slated to continue Landsat-type observations into the next decade, while the latter will provide operational continuity with MODIS. Although it may be scientifically desirable to have a constellation of high-resolution satellites giving Landsat-type observations every day or two, such a resource is unlikely in the immediate future. However, software approaches like STARFM may be able to blend aspects of coarse and fine-resolution sensors to accomplish many of the same observational goals at present.

REFERENCES

[1] J. Townshend, C. Justice, W. Li, C. Gurney, and J. McManus, "Global land cover classification by remote sensing: Present capabilities and future possibilities," *Remote Sens. Environ.*, vol. 35, no. 2/3, pp. 243–255, 1991.

[2] T. R. Loveland and D. M. Shaw, "Multi-resolution land characterization: Building collaborative partnerships," in *GAP Analysis: A Landscape Approach to Biodiversity Planning*, J. M. Scott, T. H. Tear, and F. W. Davis, Eds. Bethesda, MD: Amer. Soc. Photogramm. Remote Sensing, 1996, pp. 79–85.

[3] J. E. Vogelmann, S. M. Howard, L. Yang, C. R. Larson, B. K. Wylie, and J. N. Van Driel, "Completion of the 1990's national land cover data set for the conterminous United States from Landsat Thematic Mapper data and ancillary data sources," *Photogramm. Eng. Remote Sens.*, vol. 67, no. 6, pp. 650–662, Jun. 2001.

[4] J. G. Masek, E. F. Vermote, N. E. Saleous, R. Wolfe, F. G. Hall, F. Huemmrich, F. Gao, J. Kutler, and T. K. Lim, "A Landsat surface reflectance data set for North America, 1990–2000," *IEEE Geosci. Remote Sens. Lett.*, vol. 3, no. 1, pp. 69–72, Jan. 2005.

[5] J. Núñez, X. Otazu, O. Fors, A. Prades, V. Palà, and R. Arbiol, "Multiresolution-based image fusion with additive wavelet decomposition," *IEEE Trans. Geosci. Remote Sens.*, vol. 37, no. 3, pp. 1204–1211, May 1999.

[6] D. A. Yocky, "Multiresolution wavelet decomposition image merger of Landsat Thematic Mapper and SPOT panchromatic data," *Photogramm. Eng. Remote Sens.*, vol. 62, no. 9, pp. 1067–1074, 1996.

[7] V. K. Shettigara, "A generalized component substitution technique for spatial enhancement of multispectral images using a higher resolution data set," *Photogramm. Eng. Remote Sens.*, vol. 58, no. 5, pp. 561–567, 1992.

[8] E. F. Vermote, N. El Saleous, and C. Justice, "Atmospheric correction of the MODIS data in the visible to middle infrared: First results," *Remote Sens. Environ.*, vol. 83, no. 1, pp. 97–111, Nov. 2002.

[9] C. B. Schaaf, F. Gao, A. H. Strahler, W. Lucht, X. Li, T. Tsang, N. C. Strugnell, X. Zhang, Y. Jin, J.-P. Muller, P. Lewis, M. Barnsley, P. Hobson, M. Disney, G. Roberts, M. Dunderdale, C. Doll, R. d'Entremont, B. Hu, S. Liang, and J. L. Privette, "First operational BRDF, Albedo and Nadir reflectance products from MODIS," *Remote Sens. Environ.*, vol. 83, no. 1/2, pp. 135–148, Nov. 2002.

Feng Gao (M'99) received the B.A. degree in geology and the M.S. degree in remote sensing from Zhejiang University, Hangzhou, China, in 1989 and 1992, respectively, the Ph.D. degree in geography from Beijing Normal University, Beijing, China, in 1997, and the M.S. degree in computer science from Boston University, Boston, MA, in 2003.

From 1992 to 1998, he was a Research Assistant at the Nanjing Institute of Geography and Limnology, Chinese Academy of Science, Nanjing, China. From 1998 to 2004, he was a Research Associate Professor at the Department of Geography and a Researcher in the Center for Remote Sensing, Boston University. In August 2004, he joined the Goddard Space Flight Center through a contract with Earth Resources Technology Inc., Jessup, MD. His recent research interests include remote sensing modeling, multisensor data fusion, and retrieving vegetation parameters through inversion of remote sensing models.

Jeff Masek received the B.A. degree in geology from Haverford College, Haverford, PA, in 1989, and the Ph.D. degree in geological sciences from Cornell University, Ithaca, NY, in 1994.

He is currently a Research Scientist in the Biospheric Sciences Branch, National Aeronautics and Space Administration Goddard Space Flight Center, Greenbelt, MD. His research interests include mapping land-cover change in temperate environments, application of advanced computing to remote sensing, and satellite remote sensing techniques. He also serves as Deputy Project Scientist for the Landsat Data Continuity Mission and has held previous positions at University of Maryland, Hughes Information Systems, and Cornell University.

Matt Schwaller received the B.A. degree in biology from the State University of New York, Binghamton, the M.S. degree in remote sensing and the Ph.D. degree in natural resources both from the University of Michigan, Ann Arbor.

He was, until recently, the Data Systems and Operations Manager for the Landsat Data Continuity Mission of NASA's Goddard Space Flight Center (GSFC), Greenbelt, MD. He is currently the Ground Validation Development Manager for the Global Precipitation Measurement Mission, which is in formulation at NASA GSFC.

Forrest Hall is currently with the Goddard Space Flight Center, University of Maryland, Baltimore County Joint Center for Earth Systems Technology. He was with NASA from 1963 to 1999. Trained as a physicist, he has been active in many areas of space research. In the early 1960s, he worked with the Mercury and Apollo space mission design teams designing docking hardware for the Apollo and landing gear for the Lunar Excursion Module that landed on the lunar surface. In the late 1960s, he served on the Apollo Lunar Surface Experiment Package Team analyzing data to monitor the lunar surface and atmosphere. In the early 1970s, he began developing techniques to identify and measure agricultural crop area and productivity. He served as a Project Scientist on the Large Area Crop Inventory Experiment, which is a NASA/USDA/NOAA project to estimate global wheat production, and as the Supporting Research Manager of AgRiSTARS, which is a joint NASA/USDA project to use remote sensing to monitor global food production for other crops as well. These technologies have since been transferred to the USDA and are used in routine operational crop monitoring. For the past 26 years, he has been active in the utilization of Earth-observing satellites to monitor human-induced and natural changes to the Earth's land ecosystems and the effects those changes have had on the Earth's climate. He has served as the Project Manager of two major field campaigns, FIFE in the U.S. and BOREAS in Canada, to study the interactions between the Earth's land surface and atmosphere using satellite remote sensing. He is currently engaged in research to understand the Earth's global carbon cycle and its relationship to climate change.